Interrelation between the Portevin Le-Chatelier effect and necking in AlMg alloys

Daria Zhemchuzhnikova, Mikhail Lebyodkin, D. Yuzbekova, Tatiana Lebedkina, A. A Mogucheva, R. Kaibyshev

Interrelation between the Portevin Le-Chatelier effect and necking in AlMg alloys

Article *in* International Journal of Plasticity · June 2018

DOI: 10.1016/j.ijplas.2018.06.012

6 authors, including:

Daria Zhemchuzhnikova
Belgorod State University
30 PUBLICATIONS **137** CITATIONS
SEE PROFILE

Mikhail Lebyodkin
French National Centre for Scientific Research
115 PUBLICATIONS **1,888** CITATIONS
SEE PROFILE

Tatiana Lebedkina
University of Lorraine
61 PUBLICATIONS **808** CITATIONS
SEE PROFILE

A. A. Mogucheva
Belgorod State University
48 PUBLICATIONS **249** CITATIONS
SEE PROFILE

Manuscript: International Journal of Plasticity 110 (2018) 95–109
DOI: https://doi.org/10.1016/j.ijplas.2018.06.012

Interrelation between the Portevin Le-Chatelier effect and necking in AlMg alloys

D. Zhemchuzhnikova[a*], M. Lebyodkin[a], D. Yuzbekova[b], T. Lebedkina[a,c], A. Mogucheva[b], R. Kaibyshev[b]

[a] Laboratoire d'Etude des Microstructures et de Mécanique des Matériaux (LEM3), CNRS, Université de Lorraine, Arts & Métiers ParisTech, F-57000 Metz, France
[b] Laboratory of the Mechanical Properties of Nanoscale Materials and Superalloys, Belgorod State University, Pobedy str. 85, Belgorod 308015 Russia
[c] Togliatti State University, Belorusskaya St. 14, Tolyatti 445020, Russia

*Corresponding author: daria.zhemchuzhnikova@univ-lorraine.fr

ABSTRACT

Plastic flow instability caused by the Portevin Le-Chatelier (PLC) effect and its influence on the necking instability were studied in a binary and a precipitation-strengthened AlMg alloy using the digital image correlation (DIC) technique. Coarse-grained structure and two different fine-grained states distinctly distinguished by dislocation density were produced in both alloys using similar routes of thermomechanical processing. The patterns of stress serrations and strain localization observed at different strain rates include virtually all common types of behavior of the PLC effect. Besides, particular spatiotemporal patterns testifying to a concurrency between the propagation and localization of deformation bands are detected at low strain rates. Despite this diversity, the analysis of deformation curves with smoothened-out serrations bears evidence that the onset of necking always corresponds to the geometric Considère condition. Nevertheless, visualization of the evolution of the local strain-rate field using DIC indicates that the two mechanisms of plastic instability are closely interrelated and modify each other's behavior. The neck formation is associated with a progressive immobilization of the PLC bands, ending by the ultimate strain localization. The coexistence of two kinds of instability during necking gives rise to specific spatiotemporal patterns including oscillatory strain localization.

Keywords: Portevin-Le Chatelier effect; microstructures; metallic material; fracture mechanisms; strengthening mechanisms.

1. Introduction

Mechanical properties of alloys are strongly influenced by the macroscopic instability of uniform plastic flow, known as the Portevin–Le Chatelier (PLC) effect (Portevin and Le Chatelier, 1923). The effect manifests itself by abrupt localizations of plastic strain in transient deformation bands, giving rise to serrations on deformation curves, but also modifies overall characteristics of the material plasticity, including work-hardening behavior, ultimate tensile strength (UTS), ductility, and type of failure (Estrin and Kubin, 1995).

The microscopic mechanism of the instability is generally attributed to the so-called dynamic strain aging (DSA) of dislocations by solutes (Tamimi et al., 2015). It considers an additional barrier to the motion of dislocations, caused by the solute atoms diffusing to mobile dislocations temporarily arrested on obstacles. The strength of such additional pinning depends on the time available for solute diffusion, i.e., the waiting time for thermal activation of dislocations, and diminishes when the strain rate is increased. As a result, the steady-state strain-rate sensitivity (SRS) of the applied stress becomes negative within some strain-rate range where the waiting time and the characteristic solute diffusion time are comparable[1]. In other words, such strain-rate softening of the material is associated with an N-shaped nonlinearity. Suggesting identical conditions for all mobile dislocations, this mechanism would give rise to a periodic instability of relaxation-oscillation type, well known for dynamical systems of various nature (Ginoux and Letellier, 2012).

Real deformation curves display more complex shapes. Nevertheless, their diversity is not controlled by random deviations from this nominal behavior. Investigations on binary alloys allowed for discriminating several generic types of behavior in tension conditions (Jiang et al., 2007). Type *C* behavior is observed near the low strain-rate limit of the PLC instability and appears as deep stress drops below the nominal stress level. Therewith, subsequent bands occur in an uncorrelated manner in different cross-sections of the sample. When the applied strain rate $\dot{\varepsilon}_a$ is increased, this pattern is replaced by type *B* behavior that refers to relay-race sequences of bands, resulting in packets of stress oscillations around the nominal stress level. Type *A* behavior, associated with the high $\dot{\varepsilon}_a$ limit, corresponds to a quasi-continuous propagation of deformation bands along the tensile axis. The deformation curves display stress rises followed by backward falls at the instants of band nucleation, while irregular stress fluctuations accompany the band propagation.

This simple nomenclature is also an idealization. Not only complementary types are sometimes defined to distinguish some rarer variants of shape of deformation curves associated with the propagation mode, e.g., step-wise curves of type *D* differing from type *A* shape by the absence of stress falls (Rodriguez, 1984). Besides, real behaviors often display combinations of types, especially in practically used alloys with complex compositions and initial microstructures (Robinson, 1994; Lebedkina et al., 2014, 2017; Andreau et al., 2014; Mogucheva et al., 2016; Valdes-Tabernero et al., 2017). Such a diversity makes difficult the rationalization of various effects of the PLC instability on mechanical behavior of alloys and their relationships with the onset of necking and its progression until failure of tensile samples. The necking represents a general kind of tensile instability occurring when the plastic deformation has hardened the material so that the remaining work hardening capacity is insufficient to compensate a random reduction in the cross-section area and sustain the macroscopically uniform plastic flow. The necking condition is expressed by the well-known Considère criterion, $\Theta = \sigma$, where the work hardening rate $\Theta = d\sigma/d\varepsilon$, and σ and ε respectively denote total values of true stress and strain (Considère, 1885; Havner, 2004). When it is attained, a local increase in stress in some cross-section leads to a progressive strain localization. The end of uniform elongation thus corresponds to the maximum load, or the UTS.

Since the PLC effect causes strain localization within deformation bands, it seems natural to suggest that it may lead to a premature onset of necking. However, the literature data on the influence of the PLC effect on the necking and, more largely, failure are contradictory. Although many authors conclude on the lack of correlation between the necking onset and the PLC bands (Halim et al., 2007; Zhang et al., 2012; Jobba et al., 2015), premature failure is also reported for strain ageing alloys (Chung et al., 1977; Jobba et al., 2015; Kang et al., 2005, 2006). In (Kang et al., 2005, 2006), an early onset of necking in a AA5754 alloy deformed in type *B* conditions was interpreted from the viewpoint of the Considère strain reached locally due to strain localization within the PLC band. It should be noted however that using digital image correlation (DIC), these authors observed the development of

[1] It should be reminded that the instantaneous SRS is always positive (see, e.g., Kobelev et al., 2017).

the final shear when the PLC band met an already existing diffuse necking band. Recent investigations on a binary AlMg alloy deformed in type *A* conditions showed, on the one hand, a good agreement between the maximum load and the Considère criterion and, on the other hand, a clear correlation between the PLC bands and the onset of necking, in the sense that the latter occurred through immobilization of the last propagating PLC band, while a diffuse necking band was not observed (Yuzbekova et al., 2017). Moreover, the PLC band kept certain mobility and was decelerated progressively after the Considère condition has been reached.

These contradictions and the diversity of observations make one suggest a possible dependence of the necking process on the microstructure of alloys, in relation with the changes in the unstable plastic flow. Notably, recent studies brought evidence that precipitates and grain refinement may strongly affect both the PLC band kinematics and serration patterns (Zhemchuzhnikova, et al., 2015, 2017; Mogucheva et al., 2016; Lebedkina et al., 2017). To provide a systematic basis for investigation of the effect of the PLC bands on the neck formation, the present work is devoted to experimental studies of the onset and development of necking in two AlMg-based alloys, a binary Al-3%Mg alloy and a commercial alloy containing precipitates, in a wide strain-rate range covering different types of behavior of the PLC instability. The alloys were prepared in three microstructure conditions similar for both materials. Besides the initial coarse-grained alloy, two different fine-grained states were obtained using different routes of severe plastic deformation (Valiev and Langdon, 2006; Langdon, 2013).

2. Materials and mechanical testing

The materials investigated in this work, as well as the procedures applied to obtain severely strained conditions and characterize microstructures were described in (Yuzbekova et al., 2017) and (Nikulin et al., 2012) for the binary (hereinafter designated as A1) and commercial (A2) alloys, respectively. Below, details relevant to the present work are summarized. Table 1 specifies chemical compositions of two alloys. The initial ingots were produced by semi-continuous casting followed by homogenization annealing. No evidence of precipitation of any phase was found for the binary A1 alloy. Uniformly distributed incoherent $Al_6(Mn,Fe)$ dispersoids with an average size about 25-30 nm were detected within grain interiors in the A2 alloy.

Samples with different initial grain size were prepared from central parts of the ingots using the following procedures. Coarse-grained (CG) material was obtained by cold rolling with a total reduction of 70%, followed by annealing (2h/400°C). This processing resulted in a uniform structure of equiaxed grains with an average size about 40 μm and 15 μm for A1 and A2 alloys, respectively (Table 2). The density of lattice dislocations was inferior to 10^{13} m^{-2} in both alloys.

To produce fine-grained materials, further denoted as FG, 20 × 20 × 100 mm^3 rods were subjected to 12 passes of equal channel angular pressing (ECAP) via route B_C (Valiev and Langdon, 2006). For the A2 alloy, all ECAP passes were performed at 300°C. The A1 alloy was pressed 8 times at 300°C and 4 times at 200°C. For both materials, ECAP resulted in a uniform microstructure, with an order of magnitude increase in the lattice dislocation density. The A2 alloys displayed equiaxed grains. The recrystallization was less complete in the A1 alloy, as evident from the comparison of the fractions of high-angle boundaries (HABs, intergrain misorientation >15°) in Table 2. This material showed elongated grains with a similar transverse size, subdivided into equiaxed crystallites by low-angle boundaries (LABs), and some remnants of coarser grains (Yuzbekova et al., 2017).

Half of these billets were additionally cold rolled with a total reduction of 80% to obtain an extremely hardened material. This processing resulted in an elongation of grains along the rolling direction and an increase in the lattice dislocation density up to 10^{15} m^{-2} for both alloys. To underline the associated strain hardening effect, this material state is designated as FGH.

Dog-bone shaped tensile specimens with a 35×7×3 mm^3 gage part were cut parallel to the last deformation axis, i.e., the ECAP extrusion axis or the rolling direction. Room temperature tensile tests were performed with a constant grip velocity corresponding to the initial $\dot{\varepsilon}_a$ taking on the values of 2.86×10^{-5} s^{-1}, 1.43×10^{-4} s^{-1}, 1×10^{-3} s^{-1}, 5×10^{-3} s^{-1}, and 1.43×10^{-2} s^{-1}. DIC technique with a spatial

resolution about 25 pixels/mm and image acquisition rate of 15 frames/s was used to visualize the PLC bands (Benallal et al, 2008; Swaminathan et al., 2015; Cai et al. 2016; Yuzbekova et al., 2017). The 2D version of this technique reconstructs the evolution of the surface local strain field by correlation of successive images of a speckle pattern painted on the surface of the undeformed specimen. The calculations were performed using Vic-2D correlation software (Vic-2D system). The strain data were numerically differentiated with respect to time to obtain the corresponding local strain-rate values. Besides, since the field of vision of the camera allowed for surveying the entire gage length, the DIC data provided a precise measurement of the total strain for the analysis of the Considère condition.

To synchronize the images with the deformation curves, the output signal of the load cell of the deformation machine was also sent to an external device coupled with the DIC system camera and recording the load signal simultaneously with the camera taking images. Since the accuracy of this device was inferior to that of the load cell, the (postmortem) synchronization of two stress-time curves took use of some well-defined events, such as the abrupt stress fall at the specimen failure and deep stress drops. The matching quality is illustrated in Fig. 1a representing a series of type *B* serrations. It is seen that the instants corresponding to the onset and termination of each serration coincide for two curves within the accuracy determined by the imaging rate.

The three charts of Fig. 1 also qualify the image acquisition frequency regarding the details of stress fluctuations at different $\dot{\varepsilon}_a$. To catch rapid processes of plastic instability, the maximum imaging rate was used in all tests. The upper plot demonstrates that in not very fast tests corresponding to type *B* and type *C* (not shown) behaviors, all features of serrated deformation curves are captured by the corresponding images. Moreover, even at high strain rates (the middle and bottom charts), the acquisition frequency allows for visualizing each significant event.

3. Results

3.1. Deformation curves

Fig. 2 presents typical deformation curves of the investigated alloys in different microstructure conditions. The tensile behavior and the features of the PLC effect in the CG state of both alloys correspond to the common notions described above. Some pertinent details will be outlined here. The work-hardening evolution and the strain localization patterns will be described in the next sections. Both alloys demonstrate a yield plateau followed by a parabolic hardening. The yield plateau is usually ascribed to the propagation of the so-called Lüders band caused by a progressive unpinning of mobile dislocations from solute atmospheres in the statically aged material (Hallai and Kyriakides, 2013, Mogucheva et al., 2016, Yuzbekova et al., 2017). The dispersion-hardened A2 alloy shows a significantly higher yield and tensile strength and a slightly lower ductility than its counterpart. The families of curves obtained at different $\dot{\varepsilon}_a$ make evident a negative SRS, in conformity with the observation of plastic instability in both alloys.

The CG A1 samples show clear type *A* behavior at 5×10^{-3} s^{-1} (Fig. 2a) and 1.4×10^{-2} s^{-1} (not shown). Type *B* serrations can be recognized at large strains in the tests at 10^{-3} s^{-1} and become dominant at 1.4×10^{-4} s^{-1}. Mixed *B*+*C* serrations are observed at 2.9×10^{-5} s^{-1}. The transition to pure type *C* serrations was not complete at the lowest strain rate. Since the precipitation hardening must lead to an increase in the waiting time of dislocations on obstacles, the A2 alloy expectedly displayed a shift of the transitions between types of behavior towards higher $\dot{\varepsilon}_a$ values (cf. Mogucheva et al., 2016). As a result, all three nominal types of serration patterns have been detected (Fig. 2a'). Type *B* serrations are preponderant in the example for 10^{-3} s^{-1}. For convenience, this strain rate is utilized hereinafter as a reference value. Types *C* and *A* serrations occur, respectively, for strain rates below and above this value.

Severe plastic deformation produced similar qualitative changes in mechanical behavior of both alloys. As can be seen in Figs. 2b and 2b', ECAP leads to a significant increase in strength, effective suppression of the yield plateau, and decreases in Θ and ductility. Although a quantitative comparison of mechanical characteristics of two materials goes beyond the scope of the paper, it is noteworthy that

the changes in the strength and work hardening are stronger in the initially softer A1 alloy. According to the Considère criterion, these observations agree with a more significant ductility reduction for this material. Overall, both alloys have a similar ductility in the FG state.

The FG materials also displayed a negative SRS, although this conclusion could only be made on the overall because the scatter between samples was considerably enhanced after ECAP (e.g., curves *3* and *4* in Fig. 2b display a seemingly inversed order). Despite this uncertainty, plastic instability was observed at all strain rates. The stress serrations patterns changed significantly and showed a strong tendency to deep stress serrations with type *C* and type *B* features (cf. (Mogucheva et al. 2016)). Type *A* or type *D* behavior can be recognized at $\dot{\varepsilon}_a \geq 10^{-3}$ s^{-1} in the FG A1 alloy (e.g., curve *4* in Fig. 2b) and 1.4×10^{-2} s^{-1} in the FG A2 alloy (e.g., curve *5* in Fig. 2b')). In any case, type *B* serrations are also present from the very beginning of plastic deformation and become prevailing at large strains.

The additional cold rolling induced further changes in the average mechanical properties, which followed the same course as after ECAP. The FGH samples displayed the highest strength and the lowest values of work hardening and ductility (Figs. 2c and 2c'). Although the data scatter prevented from a quantitative comparison of the ductility, a qualitative trend to a lower ultimate elongation can be noticed for the A1 alloy. Furthermore, such extreme treatment effectively suppresses serrated behavior (cf. Lebedkina et al., 2014), in agreement with the vanishing SRS. Only sporadic serrations were observed before the onset of necking (e.g., curve *3* in Fig. 2c'). On the other hand, a transition to oscillatory behavior was detected during necking at medium and low strain rates, especially, in the A1 alloy. This transition is unusual regarding most of the literature data (see, e.g., the above citations) testifying that the instability does not change qualitatively upon the onset of necking but retains a certain continuity with the previously developed type of behavior. For example, the data of Figs. 2a–2b' attest indeed such a continuity. In contrast, curves *2* and *3* of Fig. 2c illustrate strong oscillations arising upon the onset of necking in A1 samples deformed at $\dot{\varepsilon}_a \leq 10^{-3}$ s^{-1} (cf. (Yuzbekova et al., 2017)). Weaker oscillations can also be discerned in the necking region of curves *2* and *3* obtained in similar conditions for A2 samples (Fig. 2c').

3.2. Analysis of the Considère strain

The evaluation of the work hardening in the case of unstable plastic flow needs explanation because the instantaneous rate of change of stress is virtually discontinuous at the instants of stress drops. The approach adopted in this work makes use of the fact that the Considère analysis examines the conditions of stability of the uniform plastic flow and is based on the total values of stress and strain. For this reason, the true stress-true strain curves were first smoothened and then differentiated to obtain an average work-hardening rate. Various kinds of smoothening were tested, including running average and polynomial fits, and rendered similar results, provided that the applied method efficiently removed the serrations. To compare in the same chart the results obtained for different states of the same material, the Considère criterion is represented as $n = \varepsilon$ in Fig. 3, where the work hardening index $n = d(ln\ \sigma) / d(ln\ \varepsilon) = \varepsilon \times d\sigma / (\sigma \times d\varepsilon)$. Accordingly, the Considère strain corresponds to the intersection between the straight line, $n = \varepsilon$, and the $n(\varepsilon)$ dependence calculated from the deformation curve.

Fig. 3 shows examples of verification of the Considère criterion at $\dot{\varepsilon}_a = 10^{-3}$ s^{-1}. As follows from the above description of serration patterns obtained at this reference $\dot{\varepsilon}_a$ value in different cases, this choice allows to illustrate the results of analysis for practically all types of behavior of the PLC effect. The deformation curves were fitted using a 9th order polynomial. Since the FGH A2 alloy presents a step in the middle of the deformation curve (Fig. 2c'), the origin of which will become clear in Sec. 3.3, the curve was subdivided into two parts and the calculation was performed for each part separately. The circles indicate the positions of the maximum load. They coincide very well with the intersections indicating the Considère strain. A similar correspondence was found for other $\dot{\varepsilon}_a$ values,

as well. It can thus be concluded that despite the discontinuous nature of plastic flow, the onset of necking is well determined by the Considère criterion.

Some clarifications are needed to put this conclusion into a proper perspective. First, since the smoothened deformation curve passes between the local maxima and minima of stress serrations, some local maxima occurring close to the UTS may take on higher σ values than the vertex of the smooth fitting curve. That is, the absolute maximum might appear earlier than that designated by the circles in Fig. 3. Second, since the strain hardening rate is very low in FGH samples and besides, their deformation curves fluctuate, the Considère criterion may be satisfied several times before the ultimate onset of necking (see the right-hand plot). Despite this ambiguity, the visualization of the PLC bands and the development of the ultimate shear band revealed the same basic relationship between these instabilities in all conditions, as presented in the next section.

3.3. PLC bands behavior

3.3.1. CG state

Fig. 4 presents an example of DIC data illustrating propagation of a type *A* deformation band along the gage length and nucleation of the next band in a CG A1 sample tested at the reference strain rate of 10^{-3} s^{-1}. The DIC images display several typical features of type *A* bands (see also (Yuzbekova et al., 2017)). Each band is nucleated at one specimen end and propagates toward the other end. The maximum local strain rate within the deformation band exceeds $\dot{\varepsilon}_a$ several times ($\kappa = \dot{\varepsilon}_{loc} / \dot{\varepsilon}_a \approx 7$ in Fig. 4). The propagation is continuous in the sense that the band is present in each DIC image. The bands are well-contoured and inclined about 60° to the tensile axis, alternating between two symmetrical orientations. This swapping has a simple explanation in terms of the need to compensate the rotation of the specimen axis, produced by the PLC band, and keep the specimen aligned in the direction of the applied force. When the swapping takes place during one propagation event, two conjugate bands can appear simultaneously, leading to cross-shaped strain localizations (e.g., the frame at t = 37.5 s). In this case, the swapping proceeds through nucleation of a second band with a symmetrical orientation and exhaustion of the first band.

A convenient way to visualize evolution of the deformation bands during the entire test is to construct local strain-rate maps by collecting $\dot{\varepsilon}_{loc}$ data from the DIC along the vertical centerline of the specimen and plotting them as a function of time and position (cf. (Klusemann et al., 2015) for temperature maps). Fig. 5 presents results of such processing of 2550 DIC frames for the specimen of Fig. 4. The bright lines correspond to $\dot{\varepsilon}_{loc}$ exceeding $\dot{\varepsilon}_a$ and, therefore, indicate the instantaneous location of strain localization. An inclined line corresponds to a PLC band propagating along the specimen with a velocity given by the line's slope. As an example, it can be seen that in this specimen, the Lüders plateau is caused by the propagation of two successive deformation bands. The entire map displays several pertinent features of spatiotemporal behavior of the PLC effect at a relatively high strain rate. A series of type *A* bands propagate at ~1 cm/s along the specimen at early stages of deformation. Their intensity (the maximum $\dot{\varepsilon}_{loc}$ value) increases and the velocity decreases with strain (see (Yuzbekova et al., 2017) for detail). A well-known tendency to a transition from type *A* to type *B* behavior at larger strains can also be recognized as breaks in the regular continuous propagation of the bands and alternation between the upward and downward propagation of successive bands (the latter is denoted as "band reflection" in (Ait-Amokhtar and Fressengeas, 2010)).

Two striking observations concern the strain interval about the onset of necking. On the one hand, the map reveals immobilization of the last deformation band via back-and-forth movements started before the UTS. On the other hand, such movements last for some time after the onset of necking. The band is finally stabilized at the specimen cross-section where fracture will occur. The neck development manifests itself through the constantly increasing $\dot{\varepsilon}_{loc}$ in this cross-section. It can be suggested from this example that the necking is realized through progressive immobilization of a PLC

band. This picture is qualitatively different from the common mechanism of formation of a diffuse deformation band in the uniformly deforming material, which condenses into the ultimate shear band.

The above conjecture holds for all cases studied in the present work, despite distinct types of spatiotemporal behavior in different experimental conditions. Fig. 6 displays a similar strain-rate map for a higher $\dot{\varepsilon}_a$, characterized by a quasi-continuous propagation of deformation bands during the entire tensile test. Again, the necking displays continuity with the last PLC band. Since the proneness to deformation band propagation is the stronger the higher $\dot{\varepsilon}_a$, it is not surprising that instead of multiple back-and-force movements, the last PLC band continues shifting about 15 mm following the UTS, before being damped after a short backward movement. Similar observations were reported in (Yuzbekova et al., 2017; Ait-Amokhtar and Fressengeas, 2010). Fig. 6c presents a series of DIC images corresponding to the propagation of the last two PLC bands and the onset of necking. Besides completing the representation provided in Fig. 6b, it also demonstrates the necking geometry most frequently observed in the present work. It rarely occurred along a well-defined plane determined by simple shear. More often, a competition between two conjugate bands took place during necking and resulted in a complex geometry of the fracture surface (see (Kang et al., 2006; Halim et al., 2007; Hadianfard et al., 2008; Cai et al., 2016)). The systematic analysis of the fracture geometry, however, goes beyond the scope of the present paper.

Fig. 7 describes the opposite case when a decrease in $\dot{\varepsilon}_a$ below the reference strain rate gives rise to type *B* behavior. Each stress drop is produced by an individual deformation band whereas the following reloading corresponds to a roughly uniform plastic flow[2]. The intensity of strain localization within the bands is higher than for type *A* bands and corresponds to $\kappa \sim 50$. The subsequent bands form relay-race propagation series characteristic of type *B* dynamical regime. It can be seen in Fig. 7b that necking is associated with a restriction of the propagation length, leading to a damped wobbling movement. However, it does not change the basic pattern of either strain localizations or stress serrations, except for the disappearance of stress irregularities associated with the nucleation and exhaustion of relay-race sequences.

Fig. 8 presents a detailed view of such behavior at a later stage of neck development displaying the spatially stabilized strain localization. In addition to the overall strain-rate map (Fig. 8b), the evolution of κ in the corresponding cross-section is shown in Fig. 8c. Although the $\dot{\varepsilon}_{loc}$-value on the specimen centerline does not necessarily correspond to the maximum $\dot{\varepsilon}_{loc}$ within the band, this plot allows for characterization of the intermittent character of strain localization. It can be seen that $\dot{\varepsilon}_{loc}$ jumps alternate with intervals of virtually uniform plastic flow with the strain rate approximately equal to $\dot{\varepsilon}_a$. In other words, despite the stress concentration in the necked region, the intensity of strain localization does not constantly increase, as it would be observed in the absence of the PLC effect, but continues oscillating according to type *B* behavior of the PLC instability preceding the necking.

The further decrease in the $\dot{\varepsilon}_a$ down to 2.9×10^{-5} s^{-1} does not qualitatively change this behavior for CG A1 samples. The incipient transition to type *C* behavior manifests itself as a loss of correlation between PLC bands, so that the relay-race series become composed of only several PLC bands and start in visually random sites of the gage length. The visualization of the necking renders patterns similar to Figs. 7 and 8.

These descriptions fully apply to the CG A2 material, except that type *C* behavior needs some clarification. The example presented in Fig. 2a' for a deformation curve recorded at 1.4×10^{-4} s^{-1} displays long smooth portions between deep type *C* serrations before approaching the UTS. In binary alloys, such smooth deformation is known to be related to a largely uniform plastic flow. On the

[2] A closer view uncovers plastic flow heterogeneities on smaller scales. Although unconcerned with the problem in question, this aspect might shed additional light on the dynamical behavior of the PLC instability and will be discussed elsewhere.

contrary, weak propagating bands are observed in the A2 alloy during these intervals (Fig. 9). Such unusual behavior was recently reported for a similar precipitation-strengthened AlMg alloy and interpreted by suggesting that the internal stress concentration on the precipitates may support the propagation of strain localizations (Zhemchuzhnikova et al., 2015). The properties of these bands are similar to type *A* bands. Their propagation velocity is reduced in proportion to $\dot{\varepsilon}_a$ and the κ-ratio fluctuates about 5. For comparison, κ reaches about 200 within static bands giving rise to type *C* serrations (cf. (Ait-Amokhtar et al., 2006)). The described peculiarity does not change the necking onset and progressing. Indeed, as can be seen in Fig. 2a', the frequency of serrations increases and the smooth intervals vanish at larger strains. As a result, the strain localization pattern associated with the necking corresponds to the scenario presented in Figs. 7 and 8 for the CG A1 alloy tested at the same strain rate.

3.3.2. FG state

As specified in Sec. 3.1, the grain refinement does not give rise to any new type of serrations but results in a marked tendency to type *B* and type *C* behavior. This conclusion agrees with the respective changes in the strain localization patterns. Accordingly, the above examples of the PLC bands behavior and the development of necking in CG alloys cover practically all possible situations for the FG materials, too. It is noteworthy that DIC data allow for defining more precisely the behavior of the PLC effect. For example, (short) intervals of quasi-continuous band propagation are found for the FG A2 alloy at 5×10^{-3} s^{-1} although type *B* serrations dominate on the deformation curves. In FG A1 samples, quasi-continuous propagation is detected starting from the strain rate of 10^{-3} s^{-1}.

Two differences with the examples presented for the CG state should be remarked. First, the unusual propagation regime alternating with type *C* deformation bands at low strain rates (Fig. 9) is found in both A1 and A2 alloys in FG condition. Such mobile bands were tracked at the lowest $\dot{\varepsilon}_a$ in the A1 alloy, and for both 2.9×10^{-5} s^{-1} and 1.4×10^{-4} s^{-1} in the A2 alloy. Since grain boundaries can also serve as sites of stress concentration, this observation is consistent with the above hypothesis on the mechanism promoting propagation at slow deformation.

Secondly, the propagation patterns in the FG condition indicate a concurrency with the opposite trend to static strain localization suggested from the analysis of stress serrations in Sec. 3.1. Fig. 10a illustrates this feature for a strain range before necking, where the relatively smooth portions between type *C* serrations display low-amplitude stress oscillations matching a beat in the band propagation pattern. The beat is sustained during necking, as illustrated by plotting κ-value as a function of time in Fig. 10b. From the quantitative viewpoint, the beat means that $\dot{\varepsilon}_{loc}$ never drops to the level of $\dot{\varepsilon}_a$, contrarily to the case of localized deformation bands illustrated in Fig. 8, but fluctuates between higher values (cf. (Yuzbekova et al., 2017). A similar beat was also observed during necking in some high strain-rate tests, e.g., for curve *5* in Fig. 2b'.

3.3.3. FGH state

Although the deformation curves of FGH materials are quite smooth in the work-hardening region (see Sec. 3.1), the DIC analysis shows that the smoothness is not due to a uniform plastic flow but to the propagation nature of the PLC instability at all strain rates. Unexpected regarding the known behaviors of the PLC effect, this result conforms to the above-described trends caused by the microstructure strengthening. The A2 alloy demonstrates virtually the same behavior at all $\dot{\varepsilon}_a$ values, illustrated in Fig. 11 for the reference strain rate. The entire pattern can be recognized within Fig. 6 describing the propagation mode for other material states. The elastoplastic transition is associated with the nucleation of a PLC band that propagates along either a large portion or the entire gage length and is "reflected" in the opposite direction. The change in the propagation direction involves a stress rise which corresponds to the maximum load (see Fig. 3). The further propagation demonstrates the same scenario as the type *A* band in Fig. 6. Despite the already decreasing applied stress, the band continues shifting over a long distance and is finally damped to give rise to the ultimate necking. It can be seen

that at the reference strain rate, the neck development proceeds by a beat accompanied with small stress oscillations (cf. Fig. 10). Smooth deformation during necking and a continuously increasing strain localization are found at high and low strain rates.

The FGH A1 alloy showed qualitatively similar behavior (see also (Yuzbekova et al., 2017). However, some specific observations are noteworthy. First, the PLC band propagation was usually bounded by a shorter length, from one forth to half the gage length, and was less regular, in the sense that slow fluctuations in the band width and velocity led to a less monotonous (than in A2 samples) work-hardening stage of the deformation curve. The neck development at medium and low strain rates showed a stronger trend to the occurrence of a series of distinct deformation bands (see Fig. 8) instead of a beat. It is also noteworthy that in one of the tests at 2.9×10^{-5} s^{-1}, the oscillatory strain localization associated with the neck formation started away from the specimen cross-section where the propagation of the initial deformation band terminated. Such an abrupt shift of the site of nucleation of PLC bands is characteristic of type *C* behavior. As a whole, the totality of these differences suggest a stronger tendency to the propagation mode in the FGH A2 material.

4. Discussion

4.1. Fulfillment of the Considère criterion in the presence of jerky flow

The effects of precipitation and grain-boundary strengthening on mechanical properties and the PLC instability in AlMg alloys have been intensely discussed in the literature (Robinson, 1994; Joshi et al., 2009; Lebedkina et al., 2014; Mogucheva et al., 2016; Yuzbekova et al., 2017; Zhemchuzhnikova et al., 2017). The following discussion will be devoted to the relationship between the PLC effect and the necking instability. Aiming this purpose, the present work was designed to vary experimental conditions in a wide range and compare different spatiotemporal behaviors of the PLC effect from the viewpoint of both stress serration patterns and kinematics of deformation bands. Two alloys with different composition were obtained in three different microstructure conditions and tested by tension in a strain-rate range covering three orders of magnitude. The observed behaviors include well-known types (*A*, *B*, *C*, and *D*) of spatiotemporal patterns. Besides, particular patterns associated with the deformation band propagation at low strain rate are found (Zhemchuzhnikova, et al., 2015, 2017), notably during the visibly smooth deformation of FGH alloys. Despite this diversity, the analysis of the deformation curves with smoothened-out serrations bears evidence that the onset of necking corresponds well to the Considère criterion stemming from the geometric instability of the uniform plastic flow. This observation does not agree with some literature data testifying to an early onset of necking in alloys exhibiting DSA (Chung et al., 1977; Jobba et al., 2015; Kang et al., 2005, 2006). The general character of the present observations thus requires further verification. It should, however, be noted that such a discrepancy may be due to an ambiguity in the definition of the maximum load on a serrated curve. Indeed, some local maximum corresponding to a stress rise associated with the nucleation of a PLC band may exceed the vertex of the smoothened curve and lead to a conclusion on a (apparent) premature necking. In any case, the good correspondence between the Considère criterion and the UTS determined on the smoothened curves in all experimental conditions testifies to a profound role of the geometric instability.

To interpret this uniqueness, it can be remarked that the work hardening plays the same stabilizing role in the case of finite strain localizations caused by the PLC bands, as in the case of small geometric non-uniformities in the Considère analysis. Indeed, the fast straining within the PLC band must lead to an excessive hardening of the material in the respective cross-sections and force the transfer of plastic activity to other sites. The validity of the Considère criterion can be due to the fact that although the work hardening occurs locally, i.e., within the deformation bands, their displacement along the specimen, be it through a quasi-continuous propagation, a relay race, or uncorrelated jumps, provides a uniform straining on the average. In addition to this general argument, two observations can be remarked in support of it. First, both FGH materials, possessing a low work hardening capacity, do not only have a low ductility but also display fluctuations of the stress level, leading to an ambiguity in the determination of the Considère strain. Secondly, the supposed “uniformization by propagation” is

consistent with the tendency to a lower ductility of the FGH A1 alloy. Indeed, the entirety of experiments testify that the deformation band propagation is strongly impeded in the FGH A1 samples, whereas the band propagates through the whole gage length in the FGH A2 samples. Although such mesoscopic-scale experiments do not allow for judging the relevant physical mechanism explaining this difference, a reasonable hypothesis stems from the fact that both materials have the dislocation density approaching the critical value for failure of AlMg alloys with similar Mg contents, $\rho \sim 10^{15}$ m^{-2} (Jobba et al., 2015; Park and Niewczas, 2008). Thus, the dislocation hardening mechanism is close to exhaustion in both alloys. Therefore, the additional dispersion hardening in the A2 alloy may explain its advantageous ductility (Huskins et al., 2010). This reasoning is also corroborated by the observation of a stronger tendency to the deformation band propagation at low strain rate in the A2 alloys.

4.2. Interrelation between the PLC bands and necking

Although the onset of necking is well described by the Considère criterion, the results obtained bear strong evidence that the PLC bands prepare the ultimate strain localization. Indeed, regardless the material's initial microstructure, the strain rate, and the types of the characteristic spatiotemporal pattern, the same scenario of neck formation through bounding of the PLC band displacement was realized in all experiments (see strain-rate maps in Figs. 5-7, 11). No diffuse deformation band was observed prior to the ultimate strain localization in one or two intersecting shear bands. According to the progressive character of immobilization of the PLC bands, the selection of the necking site must have a dynamical character. On the one hand, the material hardening within the PLC band maintains its mobility. On the other hand, if the PLC band becomes being captured by a (random) geometrical constraint acquired in the course of plastic flow, the longer it passes in the constraint region, the more powerful becomes the constraint itself due to the resulting reduction in the cross-section area.

The evolution of the PLC band after the UTS is reached (and before its complete immobilization) testifies that the concurrency between the necking development and the attempts of the PLC band to leave the localization site may last quite a long time (Figs. 5-7, 11). As unexpected as it could have seemed, this observation agrees with the well-known property of the slow rate of neck development, which allows for a significant straining before fracture. A more surprising observation concerns its intermittent character. It is particularly evident in the case of type *B* or type *C* behavior characterized by series of (correlated or not) static bands. It occurs that when the banding is already arrested in one region, the further necking process does not become continuous but inherits the intermittent nature of the PLC effect (Figs. 7, 8). Such intermittence can be explained by the abrupt unloading caused by the PLC bands, leading to a temporary interruption of the fast straining and its resuming upon reloading. In some cases, the unloading does not fully stop the localized straining, and the local strain-rate pattern is transformed into a beat (Figs. 10, 11). It can be concluded on the whole that the necking and the PLC instability coexist until fracture. In particular, this process gives rise to stress oscillations on the descending part of the (engineering) deformation curve. Such a persistence of the PLC instability and its coexistence with the necking instability did not receive a deserved attention from researchers so far. Nevertheless, the fact that undulatory deformation curves are systematically observed during necking (see the above references) testifies to a common character of this behavior. It is noteworthy in this context that the PLC effect and deformation band propagation were also reported for notched specimens where the strain non-uniformity was imposed by the initial specimen geometry (Graff et al., 2004).

Whereas the above discussion was mostly concentrated on the influence of the PLC instability on necking, the data also demonstrate the inverse influence. It is the most obvious in the tests on the FGH A1 samples deformed at intermediate strain rates. Indeed, in this case, the quasi-continuous propagation of a PLC band related to a smooth flow before necking is substituted with an intermittent strain localization and oscillations on the deformation curve. In other words, the strain localization imposed by the necking instability forces a transition from the propagation to localization type of behavior of the PLC instability. The same tendency can be seen when a PLC band propagating in the

FGH A2 sample or, in a range of high strain rates, in CG and FG materials, is transformed into a beat (Fig. 11).

5. Conclusions

The DIC technique was used to investigate the PLC and necking instabilities at strain rates in the range of 10^{-5}-10^{-2} s^{-1} in binary AlMg and complex AlMgMnZr alloys before and after severe plastic deformation. The following conclusions can be drawn from the results obtained:

1. The stress serration patterns observed in coarse-grained materials and fine-grained materials obtained by ECAP cover virtually all known types of behavior of the PLC effect. The additional cold-rolling leads to an efficient suppression of stress serrations before the onset of necking in the FGH materials. Nevertheless, the DIC analysis testifies that even at low strain rates, usually characterized by deep stress drops caused by immobile deformation bands, the relatively smooth plastic flow in the FGH state is associated with the propagation of one or two deformation bands. The unusual propagation mode occurring at low strain rates is also observed during reloading after deep stress drops in the coarse grained precipitation-strengthened alloy and in both alloys subjected to ECAP.
2. Despite the ubiquitous presence of the strain-rate softening PLC instability and the diversity of behaviors of the PLC bands, the necking was never observed to onset before the Considère strain determined for smoothened deformation curves.
3. At the same time, the DIC analysis reveals a close relationship between the neck formation and the prior PLC bands. The entirety of various scenarios observed experimentally can be rationalized in a unique framework considering that the neck is formed through immobilization of the PLC bands. The process involves two concurrent trends. On the one hand, the strain produced by a PLC band must help to create conditions for the geometric instability. On the other hand, the concomitant local work hardening caused by fast straining within the PLC band maintains its propagation to the less hardened cross-sections.
4. It can be concluded that two physically different kinds of plastic instability, namely, the material-dependent strain-rate softening (the PLC effect), which leads to transient strain localizations propagating along the crystal, and the geometric instability (necking) bounding the strain localization to one site, may coexist during the neck development. Moreover, evidences are found that the two kinds of instability modify each other's behavior. In particular, the strain localization upon the onset of necking in the FGH samples forces the transition from mobile to static PLC bands giving rise to oscillatory deformation curves. More generally, the concurrency of the trends to the strain propagation and strain localization gives rise to a beat in the spatiotemporal maps.

Acknowledgments

D.Zh., D.Yu. and A.M. acknowledge with gratitude the financial support received through the Russian Science Foundation, under Grant No. 17-72-20239. M.L. and T.L. acknowledge the support by the Center of Excellence "LabEx DAMAS" (Grant ANR-11-LABX-0008-01 of the French National Research Agency).

References

Ait-Amokhtar, H., Fressengeas, C., 2010. Crossover from continuous to discontinuous propagation in the Portevin–Le Chatelier effect. Acta Mater 58, 1342–1349. https://doi:10.1016/j.actamat.2009.10.038.

Ait-Amokhtar, H., Vacher, P., Boudrahem, S., 2006. Kinematics fields and spatial activity of PortevineLe Chatelier bands using the digital image correlation method. Acta Mater 54, 4365–4371. http://dx.doi.org/10.1016/j.actamat.2006.05.028.

Andreau, A., Gubicza, J., Zhang, N.X., Huang, Y., Jenei P., Langdon T.G., 2014. Effect ofshort-term annealing on the microstructures and flow properties of an Al–1%Mg alloy processed by high-pressure torsion. Mater. Sci. Eng. A 615, 231–239. http://dx.doi.org/10.1016/j.msea.2014.07.018.

Benallal, A., Berstad, V, Børvik, T., Hopperstad, O.S., Koutiri, I., Nogueira de Codes, R., 2008. Int. J. Plast. 24, 1916–1945. http://dx.doi.org/ 10.1016/j.ijplas.2008.03.008.

Cai, Y.L., Yang, S.L., Wang, Y.H., Fu, S.H., Zhang, Q.C., 2016. Characterization of the deformation behaviors associated with the serrated flow of a 5456 Al-based alloy using two orthogonal digital image correlation systems. Mater. Sci. Eng. A 664, 155–164. http://dx.doi.org/10.1016/j.msea.2016.04.003.

Chung, N., Embury, J.D., Evenson, J.D., Hoagland, R.G., Sargent, C.M., 1977. Unstable shear failure in a 7075 aluminum alloy. Acta Metall. 25, 377–381. https://doi.org/10.1016/0001-6160(77)90229-2.

Considère, A.G., 1885. Mémoire sur l'emploi du fer et de l'acier dans les constructions. Ann. des Ponts Chausses 6 (9), 574–775.

Estrin, Y., Kubin, L.P., 1995. Spatial coupling and propagative plastic instabilities, in: Mühlhaus, H.-B. (Ed.), Continuum models for materials with microstructure, John Wiley & Sons Ltd., pp. 395–450.

Ginoux, J.-M., Letellier, C., 2012. Van der Pol and the history of relaxation oscillations: Toward the emergence of a concept. Chaos 22, 023120(15). http://dx.doi.org/10.1063/1.3670008.

Graff, S., Forest, S., Strudel, J.-L., Prioul, C., Pilvin, P., Béchade, J.-L., 2004. Strain localization phenomena associated with static and dynamic strain ageing in notched specimens: experiments and finite element simulations. Mater. Sci. Eng. A 387–389, 181–185. http://dx.doi.org/10.1016/ j.msea.2004.02.083.

Hadianfard, M.J., Smerd, R., Winkler, S., Worswick, M., 2008. Effects of strain rate on mechanical properties and failure mechanism of structural Al–Mg alloys. Mater. Sci. Eng. A 492, 283–292. http://dx.doi.org/10.1016/j.msea.2008.03.037.

Hallai, J.F., Kyriakides, S., 2013. Underlying material response for Lüders-like instabilities. Int. J. Plast. 47, 1e12. http://dx.doi.org/10.1016/j.ijplas.2012.12.002.

Halim, H., Wilkinson, D.S., Niewczas, M., 2007. The Portevine-Le Chatelier (PLC) effect and shear band formation in an AA5754 alloy. Acta Mater 55, 4151–4160. http://dx.doi.org/10.1016/j.actamat.2007.03.007.

Havner, K.S., 2004. On the onset of necking in the tensile test. Int. J. Plast. 20, 965–978. http://dx.doi.org/10.1016/j.ijplas.2003.05.004.

Huskins, E.L., Cao, B., Ramesh, K.T., 2010. Strengthening mechanisms in an Al–Mg alloy. Mater. Sci. Eng. A 527, 1292–1298. http://dx.doi.org/10.1016/j.msea.2009.11.056.

Jiang, H., Zhang, Q., Chen, X., Chen, Z., Jiang, Z., Wu, X., Fan, J., 2007. Three types of Portevin-Le Chatelier effects: experiment and modelling. Acta Mater 55, 2219–2228. http://dx.doi.org/10.1016/j.actamat.2006.10.029.

Jobba, M., Mishra, R.K., Niewczas, M., 2015. Flow stress and work-hardening behaviour of AleMg binary alloys. Int. J. Plast. 65, 43–60. http://dx.doi.org/10.1016/j.ijplas.2014.08.006.

Joshi, S.P., Eberl, C., Cao, B., Ramesh, K.T., Hemker, K. J., On the Occurrence of Portevin–Le Châtelier Instabilities in Ultrafine-Grained 5083 Aluminum Alloys. 49, 207–218. http://dx.doi.org/10.1007/s11340-008-9208-3.

Kang, J., Wilkinson, D.S., Embury, J.D., Jain, M., Beaudoin, A.J., 2005. Effect of type-B Portevin–Le Chatelier bands on the onset of necking in uniaxial tension of strip cast AA5754 sheets. Scripta Mater. 53, 499–503. http://dx.doi.org/10.1016/j.scriptamat.2005.05.010.

Kang, J., Wilkinson, D.S., Jain, M., Embury, J.D., Beaudoin, A.J., Kim, S., Mishira, R., Sachdev, A.K., 2006. On the sequence of inhomogeneous deformation processes occurring during tensile deformation of strip cast AA5754. Acta Mater 54, 209–218. http://dx.doi.org/10.1016/j.actamat.2005.08.045.

King, J.E., You, C.P., Knott, J.F., 1981. Serrated yielding and the localized shear failure mode in Al alloys. Acta Metall. 29, 1553–1566. http://dx.doi.org/10.1016/0001-6160(81)90037-7.

Klusemann, B., Fischer, G., Böhlke, T., Svendsen, B., 2015. Thermomechanical characterization of Portevin–Le Châtelier bands in AlMg3 (AA5754) and modeling based on a modified Estrin–McCormick approach. Int. J. Plast. 67, 192–216. http://dx.doi.org/10.1016/j.ijplas.2014.10.011.

Kobelev, N.P., Lebyodkin, M.A., Lebedkina T.A., 2017. Role of self-organization of dislocations in the onset and kinetics of macroscopic plastic instability. Metall. Mater. Trans. A 48, 965–974. http://dx.doi.org/10.1007/s11661-016-3912-x.

Langdon, T.G., 2013. Twenty-five years of ultrafine-grained materials: Achieving exceptional properties through grain refinement, Acta Mater. 61, 7035–7059. http://dx.doi.org/10.1016/j.actamat.2013.08.018.

Lebedkina, T.A., Lebyodkin, M.A., Lamark, T.T., Janeček, M., Estrin, Y., 2014. Effect of equal channel angular pressing on the PortevineLe Chatelier effect in an Al3Mg alloy. Mater. Sci. Eng. A 615, 7–13. http://dx.doi.org/10.1016/j.msea.2014.07.064.

Lebedkina, T.A., Zhemchuzhnikova, D.A., Lebyodkin, M.A., 2017. Correlation versus randomization of jerky flow in an AlMgScZr alloy using acoustic emission. Phys. Rev. E 97, 013001(9). http://dx.doi.org/10.1103/PhysRevE.97.013001.

Mogucheva, A., Yuzbekova, D., Kaibyshev, R., Lebedkina, T., Lebyodkin, M., 2016. Effect of grain refinement on jerky flow in an Al-Mg-Sc alloy. Metall. Mater. Trans. A 47, 2093–2106. http://dx.doi.org/10.1007/s11661-016-3381-2.

Nikulin, I., Kipelova, A., Malopheyev, S., Kaibyshev, R., 2012. Effect of second phase particles on grain refinement during equal-channel angular pressing of an Al–Mg–Mn alloy. Acta Mater. 60, 487–497. http://dx.doi.org/10.1016/j.actamat.2011.10.023.

Park, D.Y., Niewczas, M., 2008. Plastic deformation of Al and AA5754 between 4.2 K and 295 K. Mater. Sci. Eng. A 491, 88–102. http://dx.doi.org/10.1016/j.msea.2008.01.065.

Portevin, A., Le Chatelier, F., 1923. Sur un phénomène observé lors de l'essai de traction d'alliages en cours de transformation. Compt. Rend. Acad. Sci. Paris 176, 507–510.

Robinson, J.M., 1994. Serrated flow in aluminium base alloys. Int. Mater. Rev. 39, 217–227. https://doi.org/10.1179/imr.1994.39.6.217.

Rodriguez, P., 1984. Serrated plastic flow. Bull. Mater. Sci. 6, 653–663. http://dx.doi.org/10.1007/BF02743993.

Tamimi, S., Andrade-Campos, A., Pinho-da-Cruz, J., 2015. Modelling the Portevin-Le Chatelier effects in aluminium alloys: a review. J. Mech. Behav. Mater. 24(3-4), 67–78. http://dx.doi.org/10.1515/jmbm-2015-0008.

Swaminathan, B., Abuzaid, W., Sehitoglu, H., Lambros J., 2015. Investigation using digital image correlation of Portevin-Le Chatelier Effect in Hastelloy X under thermo-mechanical loading. Int. J. Plast. 64, 177–192. http://dx.doi.org/10.1016/j.ijplas.2014.09.001.

Yuzbekova, D., Mogucheva, A., Zhemchuzhnikova, D., Lebedkina, T., Lebyodkin, M., Kaibyshev, R., 2017. Effect of microstructure on continuous propagation of the Portevin-Le Chatelier deformation bands. Int. J. Plast. 96, 210–2236. http://dx.doi.org/10.1016/j.ijplas.2017.05.004.

Valdes-Tabernero, M.A., Sancho-Cadenas, R., Sabirov, I., Murashkin, M.Yu., Ovid'ko, I.A., Galvez, F., 2017. Effect of SPD processing on mechanical behavior and dynamic strain aging of an Al-Mg alloy in various deformation modes and wide strain rate range. Mater. Sci. Eng. A 696, 348–359. http://dx.doi.org/10.1016/j.msea.2017.04.024.

Valiev, R.Z., Langdon, T.G., 2006. Principles of equal-channel angular pressing as a processing tool for grain refinement. Prog. Mater. Sci. 51, 881–981. http:// dx.doi.org/10.1016/j.pmatsci.2006.02.003.

Vic-2D system. http://www.correlatedsolutions.com/vic-2d.

Zhang, F., Bower, A.F., Curtin, W.A., 2012. The influence of serrated flow on necking in tensile specimens. Acta Mater. 60, 43–50. http://dx.doi.org/10.1016/j.actamat.2011.09.008.

Zhemchuzhnikova, D.A., Lebyodkin, M.A., Lebedkina, T.A., Kaibyshev, R.O., 2015. Unusual behavior of the Portevin–Le Chatelier effect in an AlMg alloy containing precipitates. Mater. Sci. Eng. A 639, 37–41. http://dx.doi.org/10.1016/j.msea.2015.04.094.

Zhemchuzhnikova, D., Lebyodkin, M., Lebedkina, T., Mogucheva, A., Yuzbekova, D., Kaibyshev, R., 2017. Peculiar Spatiotemporal Behavior of Unstable Plastic Flow in an AlMgMnScZr Alloy with Coarse and Ultrafine Grains. Metals 7, 325(13). http://dx.doi.org/10.3390/met7090325.

Table 1. Chemical compositions of investigated alloys (in wt.%).

Alloy	Mg	Mn	Zr	Si	Fe	Al.
A1	3.0	-	-	0.04	0.06	Rest
A2	5.43	0.52	0.1	0.12	0.014	Rest

Table 2. Microstructure characteristics of the investigated alloys in different conditions: grain size (d) and fraction of high-angle boundaries (HABs)

Alloy	Material condition					
	CG		FG		FGH	
	d, µm	HABs, %	d, µm	HABs, %	d, µm	HABs, %
A1	40	47	2	37	2	40
A2	15.4	94	1	70	0.33	55

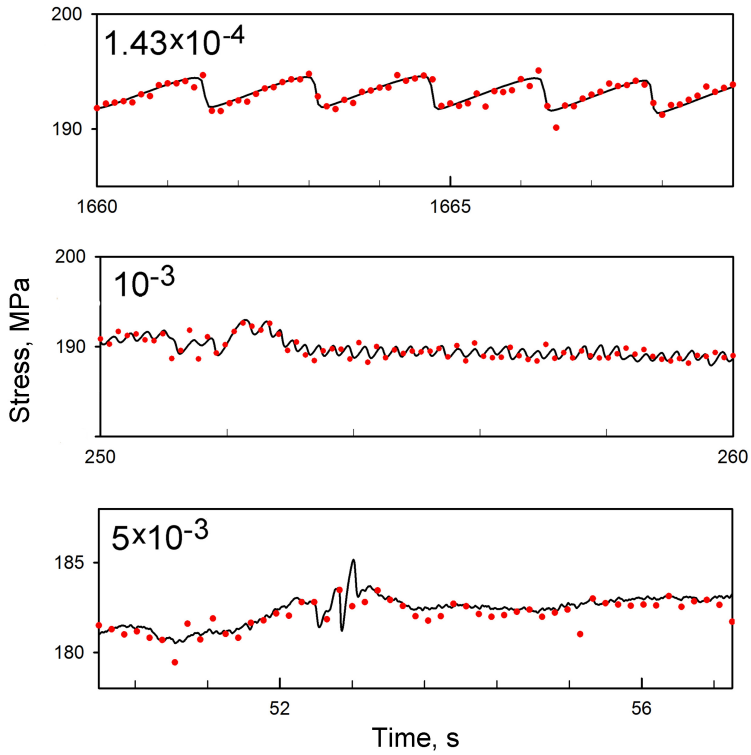

Fig. 1. Examples of synchronization of deformation curves recorded by a ZWICK testing machine (lines) and an external device coupled with the DIC system (dots). Each dot represents the instant when a DIC image is taken. Numbers designate the imposed strain rate $\dot{\varepsilon}_a$ in s^{-1}.

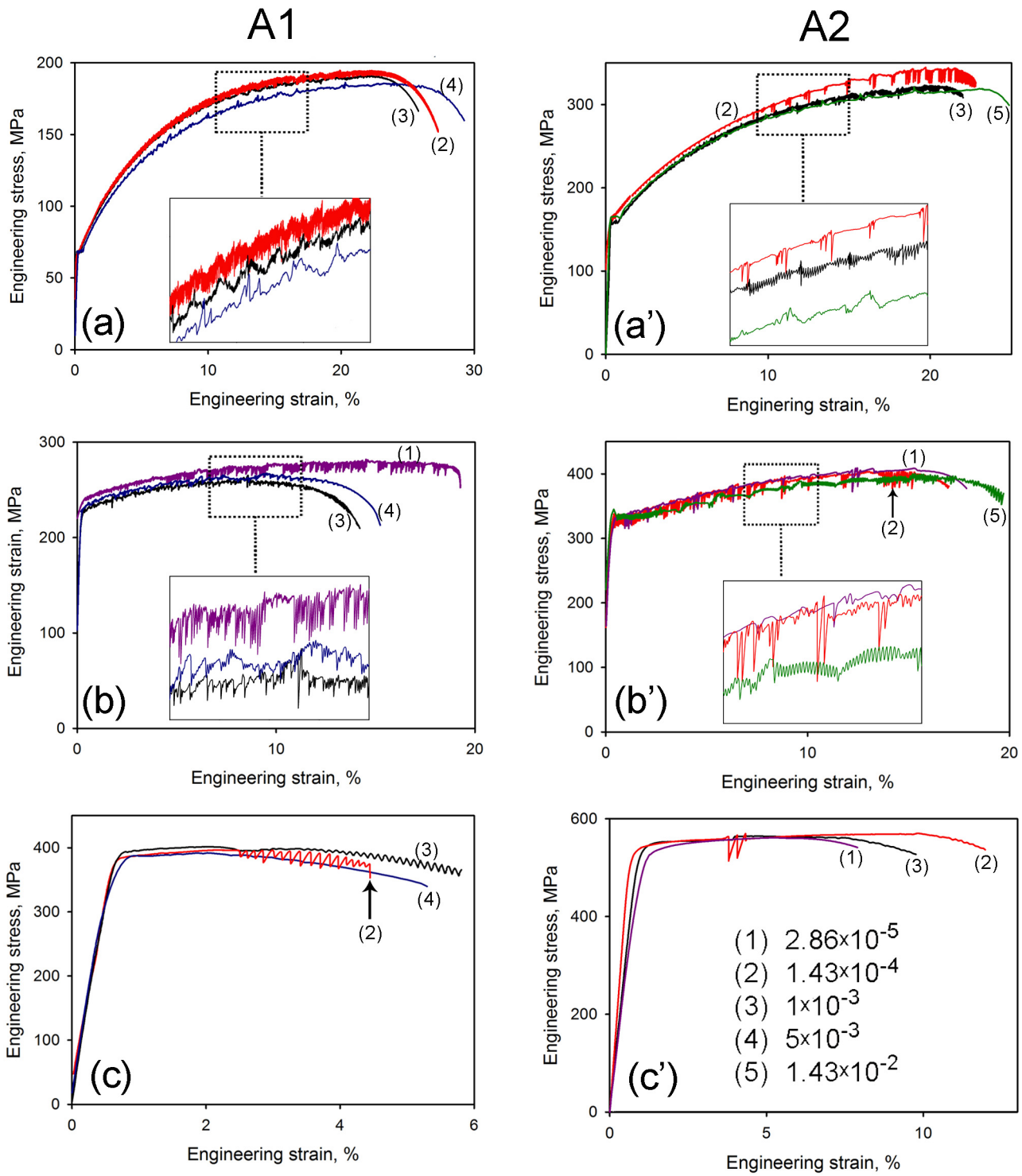

Fig. 2. Examples of engineering deformation curves for A1 (left column) and A2 (right column) alloys. (a,a') CG state; (b,b') FG state; (c,c') FGH state. The legend represents $\dot{\varepsilon}_a$ in s^{-1}. Some of the portions of the curves presented in the insets were shifted to avoid superposition and better clarify details of serrations.

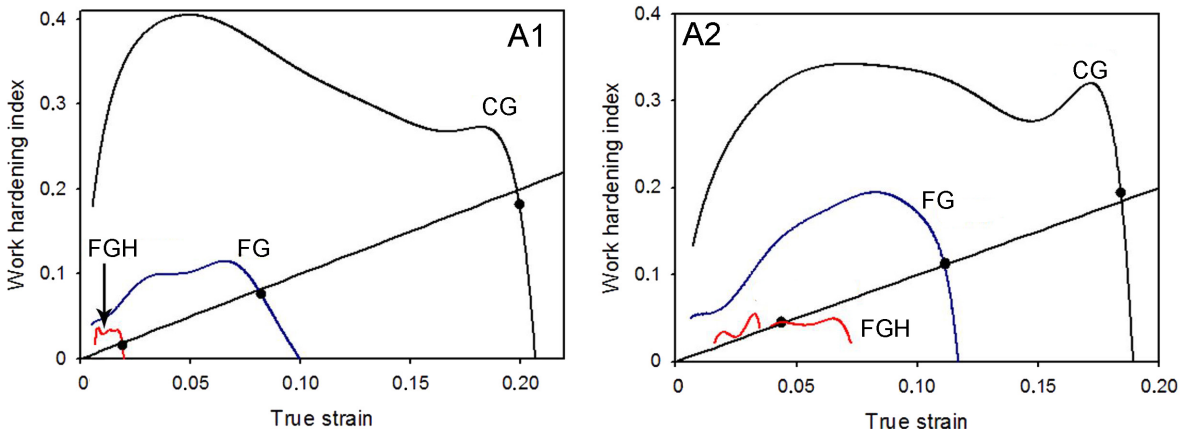

Fig. 3. Work hardening index *n* as a function of true strain ε for A1 and A2 alloys with three different initial microstructures tested at the reference strain rate of 10^{-3} s^{-1}. Strain lines correspond to the Considère criterion, $n = \varepsilon$. Black dots indicate the position of the maximum load.

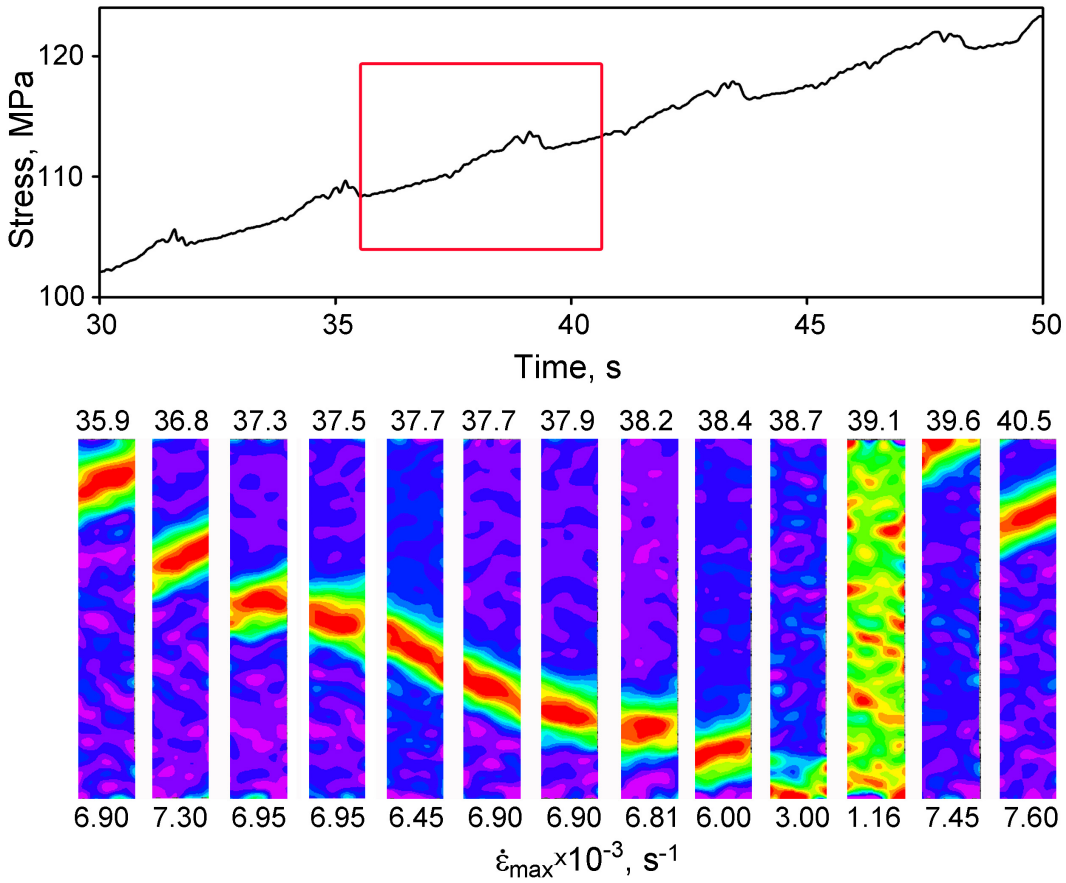

Fig. 4. Portion of a stress-time curve displaying type *A* serrations in the CG A1 alloy at 10^{-3} s^{-1} and a series of DIC images of the specimen surface, taken within the interval indicated by the rectangle. Numbers above the images specify the corresponding time instants. The image height is approximately 36 mm and corresponds to almost the entire gage length at this strain.

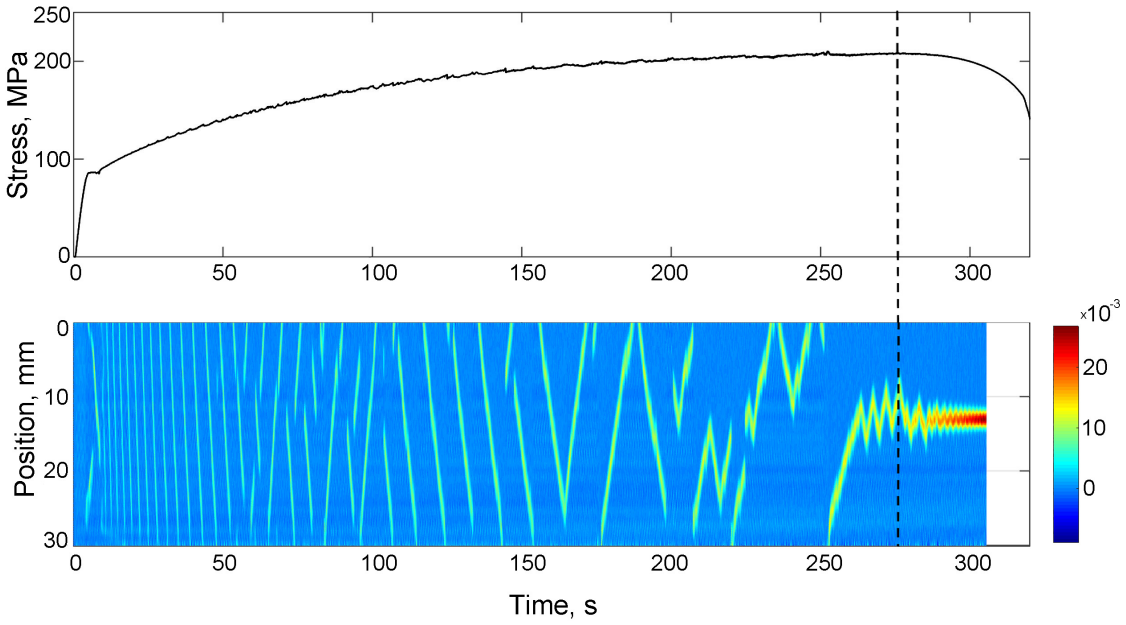

Fig. 5. The entire stress-time curve of the sample of Fig. 4 and the corresponding local strain-rate map showing the time evolution of the local strain rate along the vertical centerline (tensile axis) of the sample. The color bar represents the local strain-rate scale in s^{-1}. The vertical dashed line indicates the maximum load.

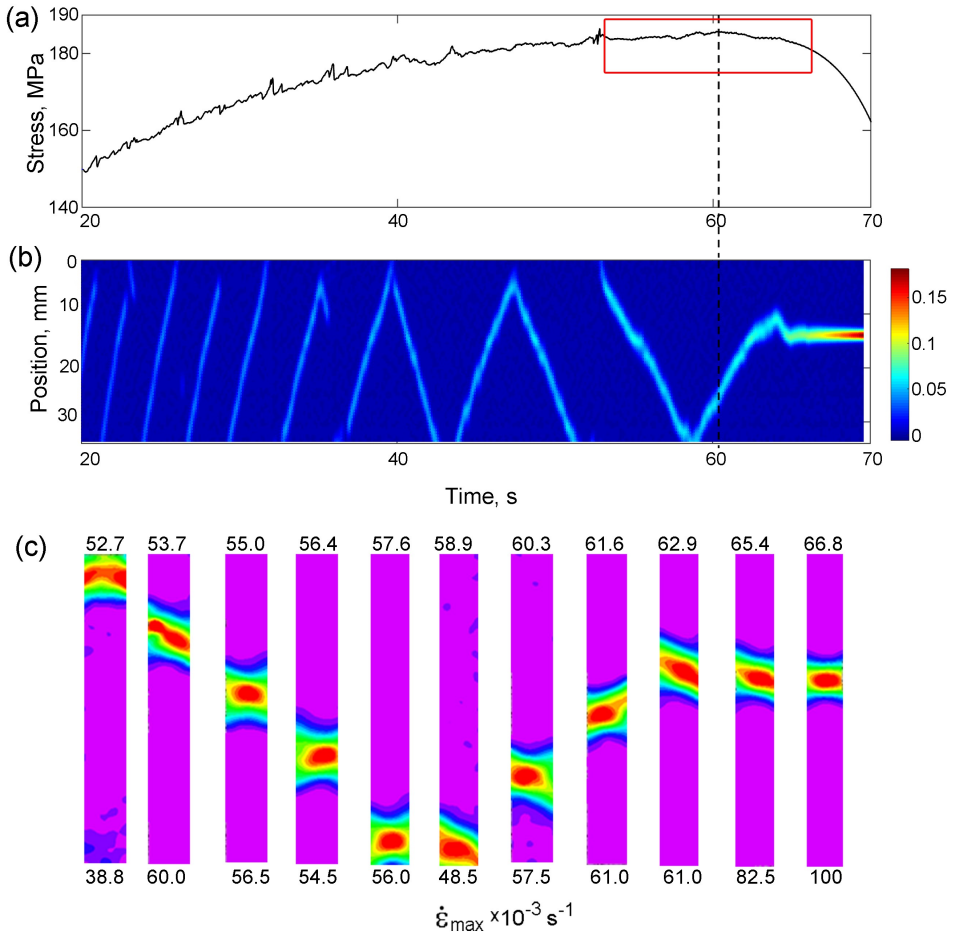

Fig. 6. (a,b) Plots similar to Fig. 5, for a CG A1 sample tested at 5×10^{-3} s^{-1}. The vertical dashed line indicates the maximum load; (c) DIC images of the specimen surface at the end of the test (see rectangle in the upper plot).

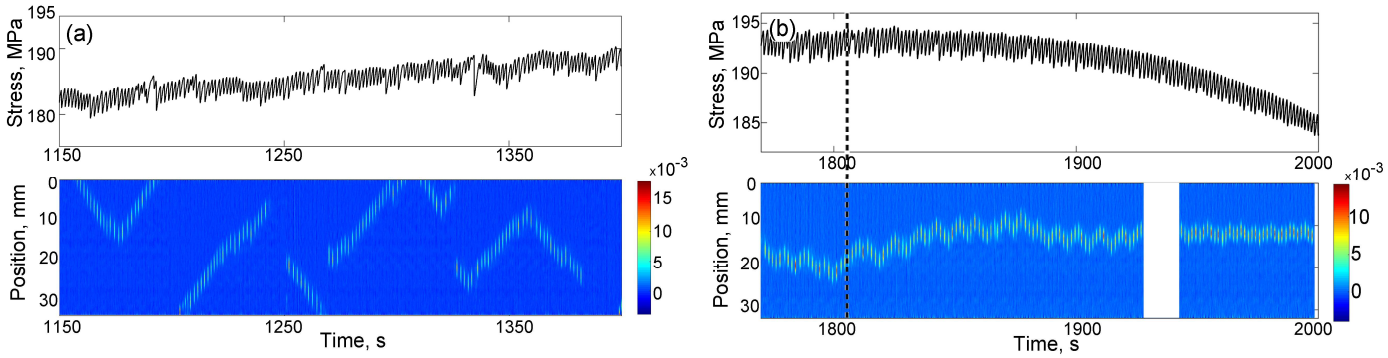

Fig. 7. Plots similar to Fig. 5, for a CG A1 sample tested at 1.43×10^{-4} s^{-1}. (a) Portion at the work-hardening stage; (b) Necking region. The vertical dashed line indicates the maximum load.

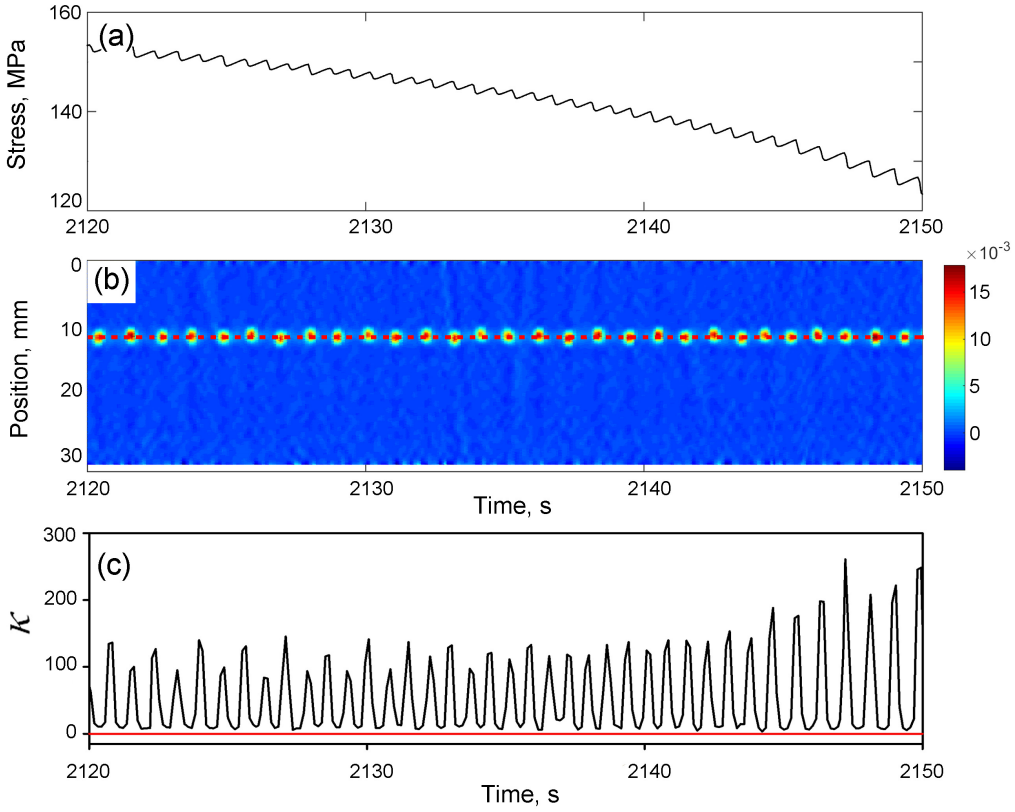

Fig. 8. (a,b) Necking development for the sample of Fig. 7 and the corresponding evolution of the value of $\kappa = \dot{\varepsilon}_{loc} / \dot{\varepsilon}_a$ in the cross-section shown by the dashed line in plot (b). The solid straight line in plot (c) presents the current value of the imposed strain rate corrected with respect to the actual specimen length.

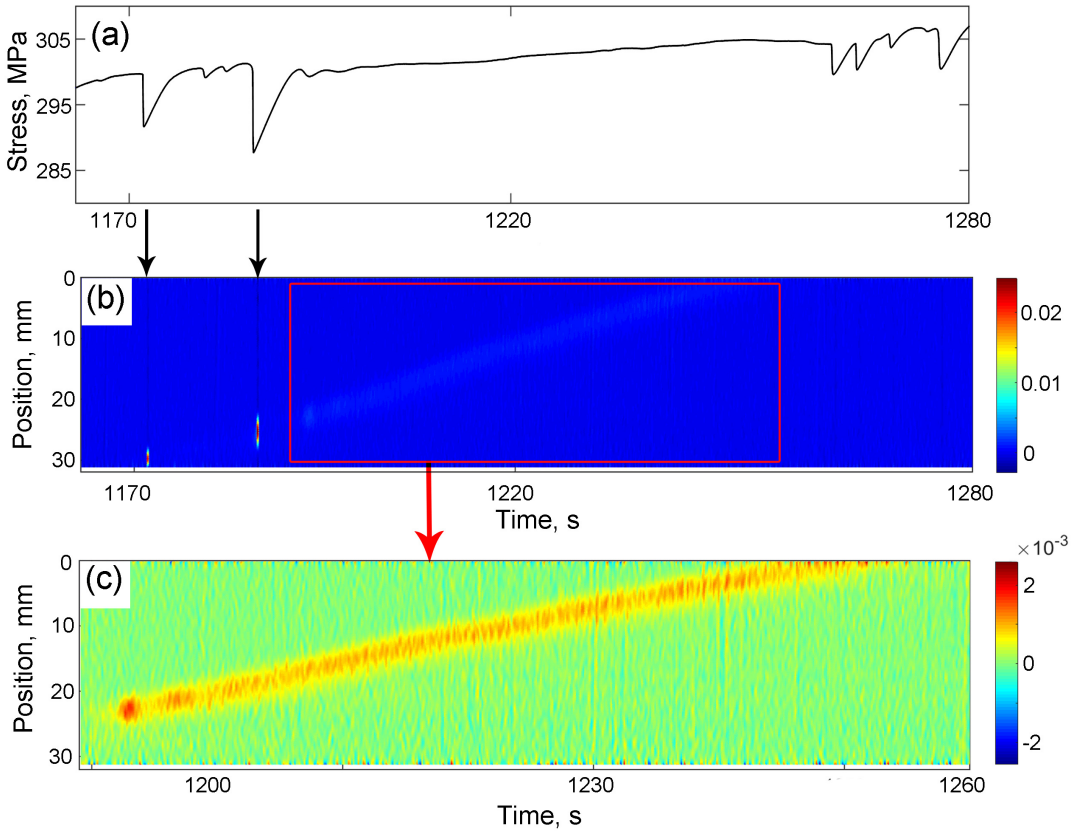

Fig. 9. (a) Stress-time curve, (b) strain-rate map, and (c) its detail showing propagation of a deformation band for a CG A2 sample tested at 1.43×10^{-4} s^{-1}.

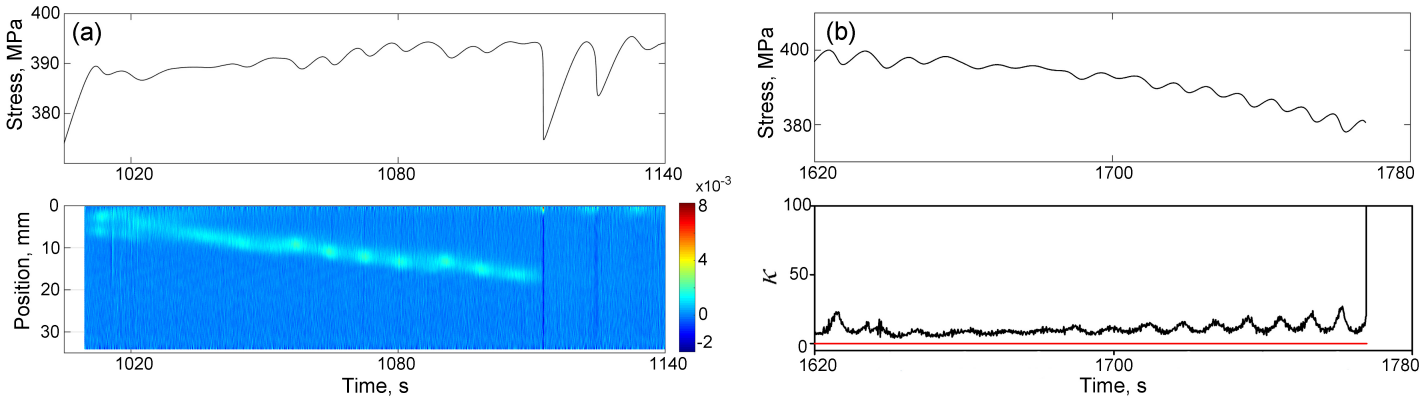

Fig. 10. (a) Portion of stress-time curve in the work-hardening region and the corresponding strain-rate map showing a beat in the band propagation pattern for a FG A2 sample tested at 1.43×10^{-4} s^{-1}. (b) Portion of stress-time curve corresponding to necking stabilized in some cross-section and the evolution of the κ-ratio in this section.

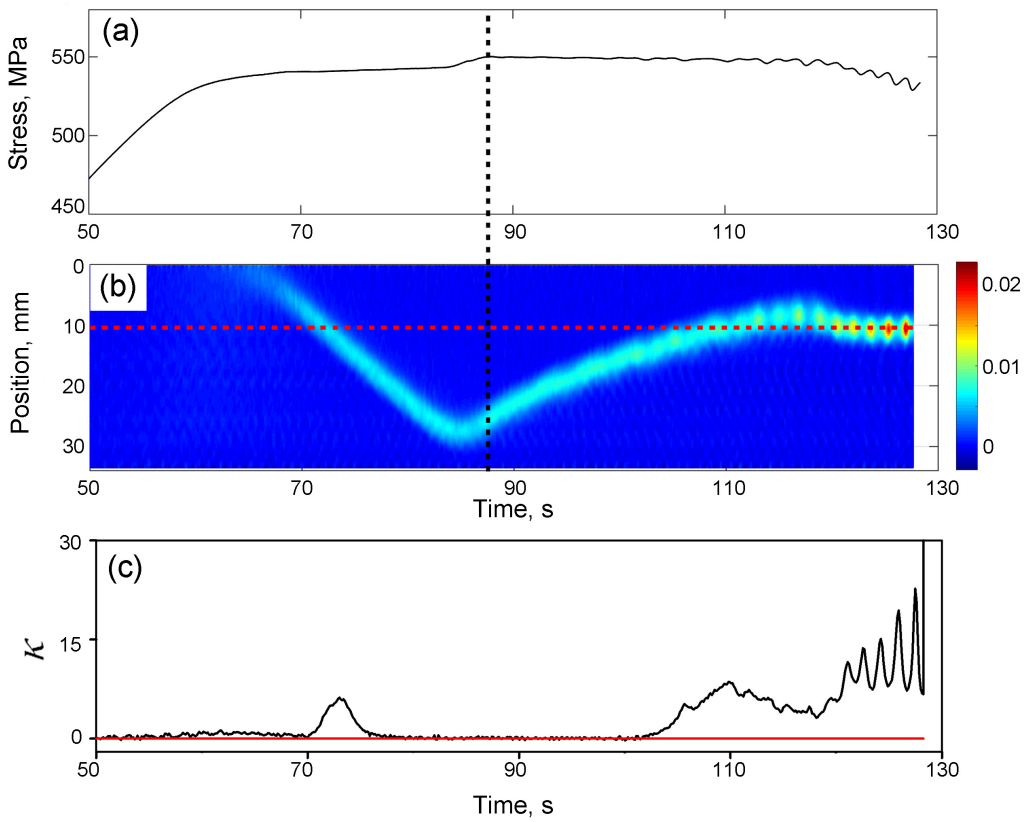

Fig. 11. Plot similar to Fig. 8, for an FGH A2 sample tested at 1×10^{-3} s^{-1}. The vertical dashed line indicates the maximum load.